A Multi-Terminal Current Differential Protection Setting Method for Fully Weak-Infeed Distribution Networks Based on Restricted Enumeration Method

Botong Li, *Member, IEEE*, Fahui Chen, Bin Li, *Senior Member, IEEE*, Jing Zhang,
Xiaotong Ji, Fan Xiao, and Qiteng Hong

Abstract—**With the high penetration connection of inverter-interfaced distributed generators and the increasing application of large-capacity energy routers, fully weak-infeed distribution networks consisting entirely of power-electronized weak-infeed power sources are set to become one of the fundamental forms of future distribution networks. For fully weak-infeed distribution networks, multi-terminal current differential protection is considered an optional or even preferred line protection scheme. In this paper, a multi-terminal current differential protection setting method for fully weak-infeed distribution networks is proposed based on the restricted enumeration method. To address the impact of data synchronization errors and measurement errors of multi-terminal current on differential current, the problem of determining the maximum differential current superimposed with the multi-terminal current phasor errors is transformed into a high-dimensional non-convex optimization problem. The distribution law of the global optimal solution in the non-convex constraint space is deeply studied and analyzed, and a restricted enumeration method is proposed that can quickly solve the protection setting value, thereby solving the problem of multi-terminal current differential protection setting. The accuracy and rapidity of the proposed method are verified by comparing the calculation accuracy and time consumption of the restricted enumeration method and the exhaustive search. It is shown that the proposed multi-terminal differential protection setting method exhibits sufficient reliability and sensitivity in fully weak-infeed distribution networks, as verified through simulation analysis using a fully weak-infeed distribution network model built in PSCAD/EMTDC.**

Index terms—**Fully weak-infeed distribution networks, multi-terminal current differential protection, restricted enumeration method, multi-terminal errors, energy router, multi-point T connection, inverter-interfaced distributed generators**

I. INTRODUCTION

Constructing a novel power system predicated on clean and low-carbon energy as its mainstay is a pivotal measure for the effective implementation of the "double carbon" strategy[1]. One of the important forms of new energy grid connection is through large-scale photovoltaic (PV), energy storage (ES), and other inverter-interfaced distributed generators (IIDGs) that are multi-point

T-connected to distribution networks (DNs)[2]. To achieve low-voltage ride-through (LVRT), IIDGs limit the magnitude of their output current during the fault ride through, which engenders typical weak-infeed properties[3-5]. Additionally, the notable benefits of a large-capacity multi-port energy router (ER) in terms of power allocation and voltage regulation render it an exemplary device to replace conventional transformers and serve as a new transmission and distribution interface[6-8]. To prevent the converter from burning during a fault, the large-capacity ER, with a modular multilevel converter (MMC) as its primary equipment, will adopt the current dependent voltage order limiter to successfully complete the fault ride through, resulting in typical weak-infeed properties[9]. Hence, the high penetration IIDGs multi-point T-connected DNs, empowered by a large-capacity ER as their transmission and distribution interface, can be categorized as fully weak-infeed distribution networks (FWIDNs), which solely rely on power electronic weak-infeed power sources.

The application of the three-step current protection and distance protection using one-terminal electrical quantities may not be appropriate in the presence of the infeed or outflowing current from multi-point T-connected IIDGs [10,11]. Additionally, the fault current characteristics of ER and IIDGs are closely tied to their fault ride-through strategies. Thus, the FWIDNs puts forward new requirements for the sensitivity and reliability of protection. Communication technology advancements and the widespread implementation of intelligent switches (ISWs) based on primary and secondary fusion technology have made current differential protection (CDP) an optional, or even preferred, line protection scheme for DNs with a high penetration of IIDGs[12]. The realization of differential protection after the integration of multi-point T-connected IIDGs into DNs has garnered significant attention in the industry. In DNs with T-connected IIDGs, double-terminal differential protection typically includes the T-connected line current into the protection action threshold, and its protection characteristics are influenced by the capacity of T-connected IIDGs. However, when the capacity of IIDGs is large, protection may fail to trip during a fault in the protection area[13]. To address this issue, Professor Y. Li proposed a solution that uses the difference between the positive sequence compensation voltages at both sides of the line as an auxiliary criterion[14]. Professor H. Li proposed a

virtual multi-terminal CDP scheme based on the use of double-terminal electrical quantities to estimate the fault current of T-connected IIDGs[15]. However, these improved double-terminal CDP principles and schemes are only applicable to power systems where the power supply is a large power supply and are not applicable in FWIDNs.

Currently, several scholars have delved into the principles and schemes of multi-terminal current differential protection (MTCDP). Based on the engineering example of DNs with teed lines, the study in paper [16] investigates the potential for data synchronization errors to cause refusal-operation and maloperation in MTCDP. Additionally, the study confirms that data synchronization errors may indeed impact the performance of MTCDP. In [17], the generalized alpha plane (GPA) formula is presented, offering the possibility of converting multi-terminal current into double-terminal current, thus enabling the use of double-terminal CDP principles in multi-terminal systems. Professor Kleber M. Silva has made enhancements to the GPA formula established in paper [17], improving the protection's sensitivity and reliability[18,19]. Senior researcher T. Wu has opted for 5G communication as the protection channel, with the multi-terminal current divided into two groups for accumulation, and then utilizing the dynamic time warping algorithm to calculate the similarity of current waveforms and determine the differential current and restraint current of MTCDP[20]. This approach has effectively addressed the problem of packet loss and bit errors in 5G communication, and reduced the impact of data synchronization errors on protection. However, none of the prior works [17-20] has thoroughly analyzed the maximum differential current superimposed with multi-terminal current phasor errors. Professor X. Lin has examined the influence of three-terminal data synchronization errors on differential current through the rho plane method[21,22]. Nevertheless, the analysis of multi-terminal data synchronization errors above three terminals through the rho plane method is too intricate to effectively gauge the influence of data synchronization errors above three terminals on differential current. This paper focuses on FWIDNs with ER and IIDG, whereas existing MTCDP methods mainly target DNs with synchronous generators (SG) as the main power sources. After a short-circuit fault, the fault current injected by SG is significantly larger than that injected by ER and IIDG. During faults outside the protected zone, the primary factor influencing the differential current is the error of the current injected by SG, while the error of the current injected by IIDG has a minimal or even negligible impact. Moreover, due to the large fault current contributed by SG, the requirement for MTCDP setting is relatively lenient. By adopting a larger reliability coefficient and protection setting value, sensitivity can still be ensured. However, in FWIDNs, the difference between the fault current and the load current is not significant, leading to small disparities in current magnitude among different terminals after a fault. Consequently, during faults outside the protected zone, the influence of current errors at each terminal on the differential current becomes non-negligible. Thus, the weak-infeed properties of FWIDNs

renders it difficult to achieve both reliability and sensitivity in MTCDP. Furthermore, existing MTCDP schemes adopt the approach of first transforming the multi-terminal currents into equivalent double-terminal currents through certain means, followed by setting double-terminal CDP with the inclusion of restraint criteria. However, these schemes lack quantitative analysis of the potential maximum differential current that might occur during external faults. Additionally, when ER and IIDG exhibit fault characteristics with limited magnitude and phase control, the selection and tuning of restraint criteria become quite challenging. Inappropriate choices could lead to large restraints during internal faults, resulting in protection maloperation. The approach of this paper is to simultaneously consider the influence of errors in multi-terminal currents on the differential current and calculate the maximum differential current during external faults, and then to set the MTCDP. The objective of this work is to establish a theoretical foundation and quantitative numerical boundaries for accurate parameter determination. Furthermore, this study aims to provide a theoretical basis for future research on methods to enhance sensitivity for internal fault detection.

This paper investigates a setting method for MTCDP in FWIDNs. Firstly, Section II delves into the weak-infeed properties of ER and IIDGs and provides a brief introduction to FWIDNs. Secondly, in Section III, the setting problem of MTCDP in FWIDNs is thoroughly analyzed, transforming the calculation of the maximum differential current with the superimposed multi-terminal current phasor error during faults outside the protected zone into a high-dimensional non-convex optimization problem. Thirdly, in Section IV, by deeply analyzing the distribution of the global optimal solution in the non-convex constraint space, a restricted enumeration method is proposed to rapidly obtain an approximate global optimal solution that satisfies the protection setting requirements. Lastly, in Section V, through a comparison of the computational results and time consumption between the restricted enumeration method and exhaustive search, the accuracy and efficiency of the proposed method are verified. A comprehensive reliability validation and sensitivity verification of the proposed protection setting method are conducted by building a FWIDNs model in PSCAD/EMTDC. The simulation includes fault scenarios inside and outside the protection zone, as well as transient events such as transformer energization and induction motor starting. By comparing the simulation results of the proposed method with those presented in references [17-20], the superior performance and effectiveness of the proposed method in FWIDNs are verified.

II. ANALYSIS OF WEAK-INFEED PROPERTIES OF ER AND IIDG

The FWIDNs with a large-capacity ER and T-connected IIDGs are shown in Fig. 1. To facilitate straightforward analysis, only the feeders under study are presented in the figure.

As depicted in Fig. 1, ES represents energy storage, PV stands for photovoltaic, and LD refers to a T-connected load.
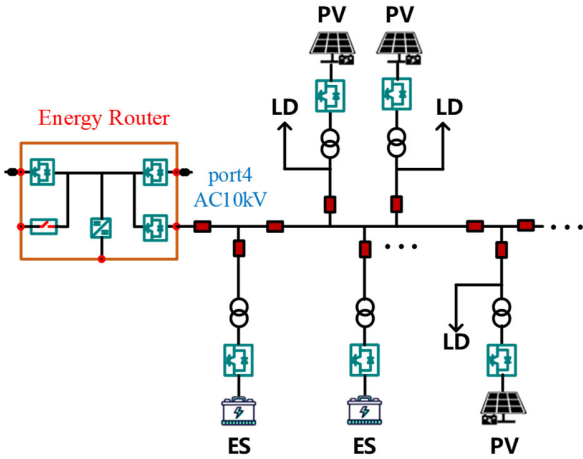
Fig. 1. Fully weak-infeed distribution networks.

IIDGs, such as PV and ES, are connected to the DNs through a teed line. Additionally, the DNs are connected to the AC 10 kV interface of the large-capacity ER. The primary components of the ER consist of DC circuit breaker, as well as MMC and associated hardware. The AC 10kV interface is connected to the AC side of MMC.

In this paper, ER serves as the system power source of the 10kV feeder. During normal operation, V/f control is adopted by MMC to support the 10 kV AC system voltage and frequency. In the event of a short-circuit fault in the DNs, MMC switches to the current dependent voltage order limiter to restrict the fault current and prevent damage or disconnection of the converter. Under the effect of the current dependent voltage order limiter[23], the fault equivalent model of ER is

$$\dot{U}_{ER} = \begin{cases} U_{ER.N} \angle (\int f_{ref} dt), & I_{ER.abc}^{max} \leq I_{cdvol}^{ref}; \\ (U_{ER.N} + kI_{cdvol}^{ref} - kI_{ER.abc}^{max}) \angle (\int f_{ref} dt), & I_{ER.abc}^{max} > I_{cdvol}^{ref}; \end{cases} \quad (1)$$

Where, $U_{ER.N}$ represents the rated voltage of the 10kV interface of ER, f_{ref} represents the rated frequency, k is the parameter for current dependent voltage order limiter, $I_{ER.abc}^{max}$ represents the maximum magnitude of the phase current among the output ABC three-phase currents of ER, and I_{cdvol}^{ref} represents the current reference value of the current dependent voltage order limiter. When $I_{ER.abc}^{max}$ is less than or equal to I_{cdvol}^{ref}, the control target for U_{ER} in the V/f control remains $U_{ER.N}$. When $I_{ER.abc}^{max}$ exceeds I_{cdvol}^{ref}, the control reference value of U_{ER} is actively reduced to limit $I_{ER.abc}^{max}$ within a certain range. Under the effect of the current dependent voltage order limiter, the fault current limitation value $I_{ER.lim}$ for ER is defined as follows.

$$I_{ER.lim} = \frac{U_{ER.N} + kI_{cdvol}^{ref}}{k} \quad (2)$$

Where, the significance of the fault current limitation value $I_{ER.lim}$ is that, in the event of a short-circuit fault, with U_{ER} and $I_{ER.abc}^{max}$ reaching a stable state, the magnitude of U_{ER} will fall between 0 and $U_{ER.N}$, while the overload level of $I_{ER.abc}^{max}$ will fall between I_{cdvol}^{ref} and $I_{ER.lim}$.

Under the LVRT control strategy and negative sequence current suppression control strategy, the T-connected IIDGs can be equivalent to a positive sequence current source controlled by the grid-connected point voltage[4]. The output current of IIDG, along with its active and reactive components, is expressed by the following equation.

$$I_q = \begin{cases} 0, & U_{pcc(1)}^* > 0.9 \\ 2(1-U_{pcc(1)}^*)I_{IIDG.N}, & 0.4 < U_{pcc(1)}^* \leq 0.9 \\ 1.2I_{IIDG.N}, & U_{pcc(1)}^* \leq 0.4 \end{cases}$$

$$I_p = \min(\frac{P_{ref}}{\sqrt{3}U_{pcc(1)}}, \sqrt{(1.2I_{IIDG.N})^2 - I_q^2}) \quad (3)$$

$$\dot{I}_{IIDG} = \sqrt{I_p^2 + I_q^2} \angle (\arctan \frac{I_q}{I_p} + \varphi)$$

Where, $U_{pcc(1)}$ represents the positive sequence voltage of the grid-connected point. $U_{pcc(1)}^*$ represents the per unit value based on the rated voltage. $I_{IIDG.N}$ represents the rated current. P_{ref} represents the active power reference value before the fault. $\dot{I}_{IIDG}$ represents the IIDG output current. I_p and I_q represent the active and reactive components of $\dot{I}_{IIDG}$, respectively. φ represents the phase of $\dot{U}_{pcc(1)}$.

As can be observed from equation (3), the output current of IIDGs displays properties of restricted magnitude and controlled phase post-fault. Through current limiting loop control, the output current of IIDGs will not surpass the rated value by more than 1.2 times, regardless of the occurrence of short-circuit faults.

In summary, DNs, featuring a large-capacity ER and T-connected IIDGs, represents a fully weak-infeed power system, in which all power sources within the network exhibit typical weak-infeed properties following short-circuit faults.

III. ANALYSIS OF MULTI-TERMINAL CURRENT DIFFERENTIAL PROTECTION SETTING PROBLEM

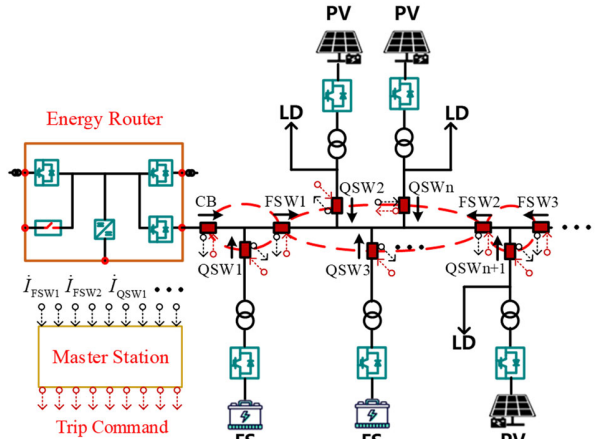The centralized MTCDP configuration scheme utilized in this paper is depicted in Fig. 2.

Fig. 2. The centralized MTCDP configuration scheme.

In Fig. 2, CB denotes the feeder outlet circuit breaker, FSW1~FSW3 represent the main line section switches, and

QSW1~QSWn+1 are the branch switches of the teed line. These switches adopt intelligent switches based on primary and secondary fusion technology, which enable electrical quantity measurement and remote control. The protection system is composed of a master station, multiple ISWs, and communication networks, and is constructed using optical fiber to ensure reliability.

The power frequency current phasor involved in a set of n ($n \geq 3$) terminal CDP can be expressed by set P

$$P = \{ \dot{I}_1, \ \dot{I}_2, \ \cdots, \ \dot{I}_n \} \tag{4}$$

The action criterion of MTCDP can be expressed as

$$I_{diff} \geq I_{set} \tag{5}$$

Where, I_{diff} is the differential current, I_{set} is the protection setting value.

Taking into account measurement errors and data synchronization errors, the relationship between the measured value and the true value of each power frequency current phasor can be expressed as

$$\dot{I}_{i.ms} = \dot{I}_{i.tr} + \Delta \dot{I}_i , i = 1, 2, \cdots, n \tag{6}$$

Where, $\dot{I}_{i.ms}$ denotes the measured value, $\dot{I}_{i.tr}$ denotes the true value, and $\Delta \dot{I}_i$ denotes the deviation between the true value and the measured value.

The differential current superimposed with multi-terminal current phasor errors is

$$I_{diff} = \left| \dot{I}_{1.ms} + \dot{I}_{2.ms} + \ \cdots \ + \dot{I}_{n.ms} \right|$$
$$= \left| \dot{I}_{1.tr} + \Delta \dot{I}_1 + \dot{I}_{2.tr} + \Delta \dot{I}_2 + \cdots + \dot{I}_{n.tr} + \Delta \dot{I}_n \right| \tag{7}$$

According to Kirchhoff's current law, the following formula holds true when the system is operating normally and a short-circuit fault occurs outside the protected zone.

$$\dot{I}_{1.tr} + \dot{I}_{2.tr} + \cdots + \dot{I}_{n.tr} = \dot{I}_C \tag{8}$$

Where, $\dot{I}_C$ represents the line capacitance current within the protection zone.

Combined (7) and (8), the differential current is

$$I_{diff} = \left| \Delta \dot{I}_1 + \Delta \dot{I}_2 + \cdots + \Delta \dot{I}_n + \dot{I}_C \right|$$
$$\leq \left| \Delta \dot{I}_1 + \Delta \dot{I}_2 + \cdots + \Delta \dot{I}_n \right| + I_C \tag{9}$$

In order to facilitate the analysis, the $\left| \Delta \dot{I}_1 + \Delta \dot{I}_2 + \cdots + \Delta \dot{I}_n \right|$ is recorded as I_{Σ}, and the maximum I_{Σ} is recorded as $I_{\Sigma.max}$.

To set the protection setting value, it is imperative to adhere to the principle of avoiding the maximum I_{diff} during external faults. Therefore, the setting be determined as follows.

$$I_{set} = k_{rel}(I_{\Sigma.max} + I_C) \tag{10}$$

Where, k_{rel} denotes the reliability coefficient, generally can take 1.1~1.3. Generally, the capacitive current per unit length of a 10kV overhead line ranges from 0.01A/km to 0.05A/km, which is small. Additionally, 10kV DNs lines are short, with lengths usually not exceeding 20km. Therefore, the capacitive current of the overhead line within the protection zone is negligible in terms of its influence on the I_{diff}. In other words, it can be approximately assumed that I_C is equal to 0. Furthermore, for urban DNs' cable lines, taking the YJY22-300mm² cable line as an example, its distributed capacitance is approximately 0.376uF/km, corresponding to a capacitance

current of about 0.68A for a 1km cable line, it also can be approximately assumed that I_C is equal to 0 when the cable lines are short. We focuses on the MTCDP of 10kV overhead lines in FWIDNs. Thus, in this paper, I_C is approximated as 0 for the analysis.

Assuming the presence of measurement error and data synchronization error, it is hypothesized that the maximum magnitude error of the power frequency current phasor is λ, and the maximum phase error is α. The specific values are determined by the current transformer model and the data synchronization accuracy of the employed method. The relationship between the $\dot{I}_{ms}$ and $\dot{I}_{tr}$ is illustrated in Fig. 3.
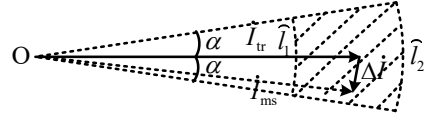
Fig. 3. The relationship between the measured value and the true value of the current phasor.

Where, the real line with arrows denotes the true value, and the dotted line with arrows denotes the measured value. $\hat{l}_1$ represents a circular arc with $(1-\lambda)I_{tr}$ as the radius and 2α as the arc center angle. Similarly, $\hat{l}_2$ represents a circular arc with $(1+\lambda)I_{tr}$ as the radius and 2α as the arc center angle. Both $\hat{l}_1$ and $\hat{l}_2$ are symmetrical about the line where $\dot{I}_{tr}$ is located. The fan-shaped shadow region represents a possible set of $\dot{I}_{ms}$.

When measurement errors and data synchronization errors coexist in n-terminal current phasors, the relationship between the measured values and the true values of the n-terminal current phasors is illustrated in Fig. 4.
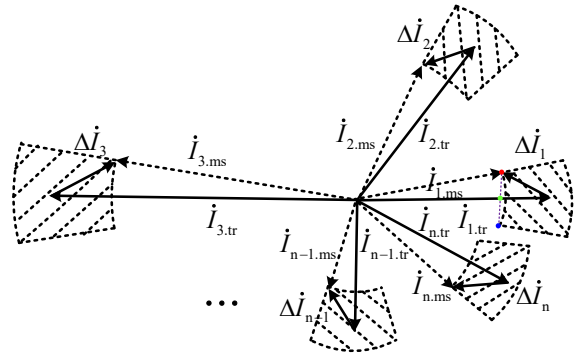
Fig. 4. The relationship between the measured values and true values of n-terminal current phasors.

It is assumed that when $\Delta \dot{I}_1 = \Delta \dot{I}_1^*$, $\Delta \dot{I}_2 = \Delta \dot{I}_2^*$, $\cdots$, and $\Delta \dot{I}_n = \Delta \dot{I}_n^*$, the I_{Σ} reaches the maximum, i.e.

$$I_{\Sigma.max} = \left| \Delta \dot{I}_1^* + \Delta \dot{I}_2^* + \cdots + \Delta \dot{I}_n^* \right| \tag{11}$$

A mathematical optimization model can be established for how to solve the $\Delta \dot{I}_1^*$, $\Delta \dot{I}_2^*$, $\cdots$, $\Delta \dot{I}_n^*$ and $I_{\Sigma.max}$. The objective function is

$$I_{\Sigma.max} = \max(\left| \Delta \dot{I}_1 + \Delta \dot{I}_2 + \cdots + \Delta \dot{I}_n \right|)$$
$$= \max(\sqrt{(\sum_{i=1}^{n} \Delta I_i \cos \varphi_{i.\Delta})^2 + (\sum_{i=1}^{n} \Delta I_i \sin \varphi_{i.\Delta})^2}) \tag{12}$$
$$= \max(f(\Delta I_1, \varphi_{1.\Delta}, \Delta I_2, \varphi_{2.\Delta}, \cdots, \Delta I_n, \varphi_{n.\Delta}))$$

Where, ΔI_i and $\varphi_{i.\Delta}$ represent the magnitude and phase of $\Delta \dot{I}_i$ ($i=1, 2, ..., n$) respectively. We can see that the mathematical optimization model contains a total of 2n variables, making it a high-dimensional optimization problem.

Based on the relationships between $\Delta \dot{I}_i$, $\dot{I}_{i.tr}$ and $\dot{I}_{i.ms}$ shown in Fig. 4, the constraint space of this mathematical optimization model can be described using the following equations.

$$\begin{cases} \dot{I}_{1.tr} + \dot{I}_{2.tr} + \cdots + \dot{I}_{n.tr} = 0 \\ 1 - \lambda_i \leq \dfrac{\left| \dot{I}_{i.tr} + \Delta \dot{I}_i \right|}{I_{i.tr}} \leq 1 + \lambda_i \\ -\alpha_i \leq \varphi_{i.ms} - \varphi_{i.tr} \leq \alpha_i \end{cases} \quad (13)$$

Where, $I_{i.tr}$ is the magnitude of $\dot{I}_{i.tr}$, $\varphi_{i.ms}$ and $\varphi_{i.tr}$ respectively denote the phases of $\dot{I}_{i.tr} + \Delta \dot{I}_i$ and $\dot{I}_{i.tr}$.

Let the feasible solutions in the constraint space be denoted as x, where x is a 2n-dimensional vector. Assuming there are two feasible solutions, $x_1 = \left[\Delta I_1', \varphi_{1.\Delta}', \Delta I_2', \varphi_{2.\Delta}', \cdots, \Delta I_n', \varphi_{n.\Delta}' \right]$ and $x_2 = \left[\Delta I_1'', \varphi_{1.\Delta}'', \Delta I_2'', \varphi_{2.\Delta}'', \cdots, \Delta I_n'', \varphi_{n.\Delta}'' \right]$. Let x_1 and x_2 have the same elements except for $\Delta I_1'$, $\varphi_{1.\Delta}'$, $\Delta I_1''$ and $\varphi_{1.\Delta}''$, where $\Delta I_1'$ and $\varphi_{1.\Delta}'$ determine the endpoint of $\Delta \dot{I}_1$ at the red point in Fig. 4, and $\Delta I_1''$ and $\varphi_{1.\Delta}''$ determine the endpoint of $\Delta \dot{I}_1$ at the blue point. The linear combination of x_1 and x_2, denoted as $x_3 = tx_1 + (1-t)x_2$, where $t \in [0,1]$. The green point in Fig. 4 represents any point on the line connecting the red and blue points, i.e., the endpoint of $\Delta \dot{I}_1$ determined by x_3. From Fig. 4, it can be observed that the green point is not within the shaded sector. Therefore, x_3 is not a solution within the constraint space. According to the definition of a non-convex space, it can be determined that the constraint space of this mathematical optimization model is a non-convex space. Hence, we conclude that this mathematical optimization problem is a non-convex optimization problem.

One approach to solving non-convex optimization problems is using convex approximation methods, where some constraints are relaxed to transform the problem into a convex optimization problem, which is then solved using convex optimization techniques. However, convex approximation methods cannot guarantee global optimal solutions (GOS) for non-convex optimization problems, nor can they guarantee the obtained approximate solutions meet the requirements of protection settings. Another approach is to use iterative non-convex optimization algorithms such as alternating minimization and stochastic optimization, but these methods are sensitive to the selection of initial values, and different initial values may yield different results. They also cannot guarantee that the solutions obtained meet the requirements of protection settings. The selection of an appropriate method for solving non-convex optimization problems should be based on the specific characteristics of the optimization model. Therefore, in order to meet the requirements of protection settings, we propose a restricted enumeration method for solving this problem, based on a thorough analysis of the distribution characteristics of the global optimal solutions of the proposed non-convex optimization problem in the non-convex space, which is elaborated in detail in Section IV.

IV. MTCDP SETTING METHOD BASED ON RESTRICTED ENUMERATION METHOD

The concept behind the restricted enumeration method is to begin by scrutinizing the distribution law of the GOS within the non-convex constraint space (NCCS). Building on this foundation, the NCCS is limited and streamlined, culminating in the implementation of an exhaustive search within a more confined constraint space.

A. Three Distribution Laws of The Global Optimal Solution in The Non-Convex Constraint Space.

The first distribution law is that the terminal points of $\Delta \dot{I}_1^*$, $\Delta \dot{I}_2^*$, $\cdots$, $\Delta \dot{I}_n^*$ lie on the boundaries of their respective fan-shaped shadow regions.

As an illustration, consider the positional relationship between $\Delta \dot{I}_1^* + \Delta \dot{I}_2^* + \cdots + \Delta \dot{I}_{n-1}^*$ and $\Delta \dot{I}_n^*$ in the complex plane as shown in Fig. 5,
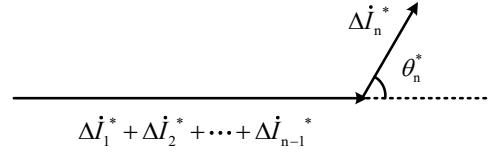

Fig. 5. The positional relationship between $\Delta \dot{I}_n^*$ and $\Delta \dot{I}_1^* + \Delta \dot{I}_2^* + \cdots + \Delta \dot{I}_{n-1}^*$ in the complex plane.

Where, θ_n^* denotes the phase difference between $\Delta \dot{I}_n^*$ and $\Delta \dot{I}_1^* + \Delta \dot{I}_2^* + \cdots + \Delta \dot{I}_{n-1}^*$, $\theta_n^* \in [0, 2\pi)$.

Based on the cosine theorem, $I_{\Sigma.max}^2$ can be expressed as

$$\begin{aligned} I_{\Sigma.max}^2 &= \left| \Delta \dot{I}_1^* + \Delta \dot{I}_2^* + \cdots + \Delta \dot{I}_{n-1}^* + \Delta \dot{I}_n^* \right|^2 \\ &= \left| \Delta \dot{I}_1^* + \Delta \dot{I}_2^* + \cdots + \Delta \dot{I}_{n-1}^* \right|^2 + \left| \Delta \dot{I}_n^* \right|^2 \\ &\quad -2 \cdot \left| \Delta \dot{I}_n^* \right| \cdot \left| \Delta \dot{I}_1^* + \Delta \dot{I}_2^* + \cdots + \Delta \dot{I}_{n-1}^* \right| \cos(\pi - \theta_n^*) \end{aligned} \quad (14)$$

The $\Delta \dot{I}_n$ whose phase is θ_n^* ahead of $\Delta \dot{I}_1^* + \Delta \dot{I}_2^* + \cdots + \Delta \dot{I}_{n-1}^*$ is denoted by $\Delta \dot{I}_n^{\theta_n^*}$. The $\Delta \dot{I}_n^{\theta_n^*}$ whose terminal point lies on the boundary of the fan-shaped shadow region is denoted by $\Delta \dot{I}_n^{\theta_n^*, \, max}$.

Given that $\Delta \dot{I}_1^*$, $\Delta \dot{I}_2^*$, $\cdots$, $\Delta \dot{I}_{n-1}^*$ and $\Delta \dot{I}_n^{\theta_n^*}$ are mutually independent, the derivative of the I_Σ^2 to the $\left| \Delta \dot{I}_n^{\theta_n^*} \right|$ is

$$\begin{aligned} \frac{d(I_\Sigma^2)}{d\left(\left| \Delta \dot{I}_n^{\theta_n^*} \right| \right)} &= 2 \left| \Delta \dot{I}_n^{\theta_n^*} \right| - 2 \cdot \cos(\pi - \theta_n^*) \\ &\quad \cdot \left| \Delta \dot{I}_1^* + \Delta \dot{I}_2^* + \cdots + \Delta \dot{I}_{n-1}^* \right| \end{aligned} \quad (15)$$

The second derivative of the I_Σ^2 to the $\left| \Delta \dot{I}_n^{\theta_n^*} \right|$ is

$$\frac{d^2(I_\Sigma^2)}{d\left(\left| \Delta \dot{I}_n^{\theta_n^*} \right| \right)^2} = 2 > 0 \quad (16)$$

By combining equations (14) to (16), we observe that the first derivative is a linear function, and the second derivative is a constant that is always greater than zero. Thus, as $\left| \Delta \dot{I}_n^{\theta_n^*} \right|$ varies from 0 to $\left| \Delta \dot{I}_n^{\theta_n^*, max} \right|$, I_Σ has at most one extremum, which is the extreme minimum point. Therefore, the maximum value of I_Σ can only be attained when $\Delta \dot{I}_n^{\theta_n^*} = 0$ or $\Delta \dot{I}_n^{\theta_n^*} = \Delta \dot{I}_n^{\theta_n^*, max}$.

Since we can always find a $\Delta \dot{I}_n$ that is in the same direction as $\Delta \dot{I}_1^* + \Delta \dot{I}_2^* + \cdots + \Delta \dot{I}_{n-1}^*$ but with a non-zero magnitude,

there must be at least one $\Delta \dot{I}_n^{\xi}$ lying within the fan-shaped shadow region that satisfies the following inequality.

$$\left| \Delta \dot{I}_1^* + \Delta \dot{I}_2^* + \cdots + \Delta \dot{I}_{n-1}^* + \Delta \dot{I}_n^{\xi} \right| \\ > \left| \Delta \dot{I}_1^* + \Delta \dot{I}_2^* + \cdots + \Delta \dot{I}_{n-1}^* + 0 \right| \tag{17}$$

Thus, the maximum value of I_Σ can only be achieved when $\Delta \dot{I}_n^{\theta_n^*} = \Delta \dot{I}_n^{\theta_n^*,\max}$.

In conclusion, when I_Σ reaches its maximum value, the terminal point of the corresponding phasor must lie on the boundary of the fan-shaped shadow region. A similar conclusion can be drawn when analyzing $\Delta \dot{I}_1^*$ to $\Delta \dot{I}_{n-1}^*$ separately.

The second distribution law states that if the terminal point of any phasor in $\Delta \dot{I}_1^*$, $\Delta \dot{I}_2^*$, $\cdots$, $\Delta \dot{I}_n^*$ lies on the straight line boundary of its fan-shaped shadow region, then the terminal point of the phasor must also lie at both ends of the straight line boundary.

As shown in Fig. 6, the four boundaries of the fan-shaped shadow region corresponding to $\Delta \dot{I}_n$ are numbered.
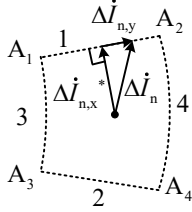

Fig. 6. Analysis diagram of the second distribution law.

Where, boundaries 1 and 2 are straight boundaries, while boundaries 3 and 4 are arc boundaries. When the terminal point of $\Delta \dot{I}_n$ is on boundary 1, $\Delta \dot{I}_n$ can be decomposed into

$$\Delta \dot{I}_n = \Delta \dot{I}_{n,x}^* + \Delta \dot{I}_{n,y} \tag{18}$$

Where, $\Delta \dot{I}_{n,x}^*$ and $\Delta \dot{I}_{n,y}$ are the projection of $\Delta \dot{I}_n$ onto the vertical line of boundary 1 and boundary 1, respectively.

When the terminal point of $\Delta \dot{I}_{n,y}$ is near side A_1, $I_{\Sigma.\max}^2$ is equal to

$$\begin{aligned} I_{\Sigma.\max}^2 &= \left| \Delta \dot{I}_1^* + \Delta \dot{I}_2^* + \cdots + \Delta \dot{I}_{n-1}^* + \Delta \dot{I}_n^* \right|^2 \\ &= \left| \Delta \dot{I}_1^* + \Delta \dot{I}_2^* + \cdots + \Delta \dot{I}_{n-1}^* + \Delta \dot{I}_{n,x}^* + \Delta \dot{I}_{n,y}^* \right|^2 \\ &= \left| \Delta \dot{I}_1^* + \Delta \dot{I}_2^* + \cdots + \Delta \dot{I}_{n,x}^* \right|^2 + \left| \Delta \dot{I}_{n,y}^* \right|^2 \\ &\quad -2 \cdot \left| \Delta \dot{I}_{n,y}^* \right| \cdot \left| \Delta \dot{I}_1^* + \Delta \dot{I}_2^* + \cdots + \Delta \dot{I}_{n,x}^* \right| \cos(\frac{\pi}{2} - \delta_n^*) \end{aligned} \tag{19}$$

Where, δ_n^* is the phase difference between $\Delta \dot{I}_{n,x}^*$ and $\Delta \dot{I}_1^* + \Delta \dot{I}_2^* + \cdots + \Delta \dot{I}_{n-1}^*$, $\delta_n^* \in [0, 2\pi)$.

Since $\Delta \dot{I}_1^*$, $\Delta \dot{I}_2^*$, $\cdots$, $\Delta \dot{I}_n^*$, $\Delta \dot{I}_{n,x}^*$ and $\Delta \dot{I}_{n,y}$ are mutually independent, the derivative of the I_Σ^2 with respect to $\left| \Delta \dot{I}_{n,y} \right|$ is

$$\begin{aligned} \frac{d(I_\Sigma^2)}{d(\left| \Delta \dot{I}_{n,y} \right|)} &= 2\left| \Delta \dot{I}_{n,y} \right| - 2\cos(\frac{\pi}{2} - \delta_n^*) \\ &\quad \cdot \left| \Delta \dot{I}_1^* + \Delta \dot{I}_2^* + \cdots + \Delta \dot{I}_{n-1}^* + \Delta \dot{I}_{n,x}^* \right| \end{aligned} \tag{20}$$

The second derivative of the I_Σ^2 with respect to the $\left| \Delta \dot{I}_{n,y} \right|$ is

$$\frac{d^2(I_\Sigma^2)}{d(\left| \Delta \dot{I}_{n,y} \right|)^2} = 2 > 0 \tag{21}$$

When the terminal point of $\Delta \dot{I}_{n,y}^*$ is near side A_2, $I_{\Sigma.\max}^2$ is

$$\begin{aligned} I_{\Sigma.\max}^2 &= \left| \Delta \dot{I}_1^* + \Delta \dot{I}_2^* + \cdots + \Delta \dot{I}_{n-1}^* + \Delta \dot{I}_n^* \right|^2 \\ &= \left| \Delta \dot{I}_1^* + \Delta \dot{I}_2^* + \cdots + \Delta \dot{I}_{n-1}^* + \Delta \dot{I}_{n,x}^* + \Delta \dot{I}_{n,y}^* \right|^2 \\ &= \left| \Delta \dot{I}_1^* + \Delta \dot{I}_2^* + \cdots + \Delta \dot{I}_{n,x}^* \right|^2 + \left| \Delta \dot{I}_{n,y}^* \right|^2 \\ &\quad -2 \cdot \left| \Delta \dot{I}_{n,y}^* \right| \cdot \left| \Delta \dot{I}_1^* + \Delta \dot{I}_2^* + \cdots + \Delta \dot{I}_{n,x}^* \right| \cos(\frac{3\pi}{2} - \delta_n^*) \end{aligned} \tag{22}$$

The derivative of the I_Σ^2 with respect to the $\left| \Delta \dot{I}_{n,y} \right|$ is

$$\begin{aligned} \frac{d(I_\Sigma^2)}{d(\left| \Delta \dot{I}_{n,y} \right|)} &= 2\left| \Delta \dot{I}_{n,y} \right| - 2\cos(\frac{3\pi}{2} - \delta_n^*) \\ &\quad \cdot \left| \Delta \dot{I}_1^* + \Delta \dot{I}_2^* + \cdots + \Delta \dot{I}_{n-1}^* + \Delta \dot{I}_{n,x}^* \right| \end{aligned} \tag{23}$$

The second derivative of I_Σ^2 with respect to $\left| \Delta \dot{I}_{n,y} \right|$ is the same as (21).

The $\Delta \dot{I}_{n,y}$ whose terminal point is at the point A_1 is denoted by $\Delta \dot{I}_{n,y}^{A1}$, and the $\Delta \dot{I}_{n,y}$ whose terminal point is at the point A_2 is denoted by $\Delta \dot{I}_{n,y}^{A2}$. The derivatives in (20) and (23) are denoted by $f_{n,y}^1$ and $f_{n,y}^2$ respectively.

Combining (19) to (23), since the first derivative is a linear function, and the second derivative is a constant that is always greater than zero, as $\left| \Delta \dot{I}_{n,y} \right|$ changes from 0 to $\left| \Delta \dot{I}_{n,y}^{A1} \right|$, I_Σ has at most one extreme point, which is the extreme minimum point. Likewise, as $\left| \Delta \dot{I}_{n,y} \right|$ changes from 0 to $\left| \Delta \dot{I}_{n,y}^{A2} \right|$, I_Σ also has at most one extreme point, which is the extreme minimum point. Therefore, the maximum value of I_Σ is possible only when $\Delta \dot{I}_{n,y} = 0$ or $\Delta \dot{I}_{n,y} = \Delta \dot{I}_{n,y}^{A1}$ or $\Delta \dot{I}_{n,y} = \Delta \dot{I}_{n,y}^{A2}$.

However, regardless of the value of δ_n^*, the following equation must be true.

$$\cos(\frac{3\pi}{2} - \delta_n^*) \cdot \cos(\frac{\pi}{2} - \delta_n^*) \le 0 \tag{24}$$

Therefore, at least one of $f_{n,y}^1$ and $f_{n,y}^2$ is greater than or equal to 0 regardless of the value of $\left| \Delta \dot{I}_{n,y} \right|$, i.e.

$$\begin{aligned} f_{n,y}^1 &= 2\left| \Delta \dot{I}_{n,y} \right| - 2\cos(\frac{\pi}{2} - \delta_n^*) \\ &\quad \cdot \left| \Delta \dot{I}_1^* + \Delta \dot{I}_2^* + \cdots + \Delta \dot{I}_{n-1}^* + \Delta \dot{I}_{n,x}^* \right| \ge 0 \\ \text{or } f_{n,y}^2 &= 2\left| \Delta \dot{I}_{n,y} \right| - 2\cos(\frac{3\pi}{2} - \delta_n^*) \\ &\quad \cdot \left| \Delta \dot{I}_1^* + \Delta \dot{I}_2^* + \cdots + \Delta \dot{I}_{n-1}^* + \Delta \dot{I}_{n,x}^* \right| \ge 0 \end{aligned} \tag{25}$$

In at least one of the two cases of $\Delta \dot{I}_{n,y} = \Delta \dot{I}_{n,y}^{A1}$ or $\Delta \dot{I}_{n,y} = \Delta \dot{I}_{n,y}^{A2}$, it has been observed that the value of I_Σ is greater than that of $\Delta \dot{I}_{n,y} = 0$. Consequently, it can be inferred that when I_Σ attains its maximum, the terminal point of ΔI_n^* would be situated on the straight boundary of the fan-shaped region. Moreover, it would be located at both ends of the straight boundary. It is evident that the same conclusion can be arrived at when analyzing $\Delta \dot{I}_1^*$ to $\Delta \dot{I}_{n-1}^*$ separately.

The third distribution law states that if the terminal points of $\Delta \dot{I}_1^*$, $\Delta \dot{I}_2^*$, $\cdots$, $\Delta \dot{I}_n^*$ are on the inner arc of the fan-shaped region, they must be located at both ends of the inner arc. However, if they are on the outer arc of the fan-shaped region,

they may appear anywhere on the outer arc.

To illustrate this point, let us consider $\Delta \dot{I}_n{}^*$. By connecting A_1A_3 and A_2A_4, we can analyze the distribution law of the GOS on the inner and outer arcs of the fan-shaped region, as depicted in Fig. 7.
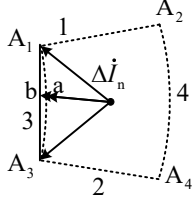

Fig. 7. Analysis diagram of the third distribution law.

As shown in Fig. 7, point a represents any point on the boundary 3. By extending $\Delta \dot{I}_n$ whose terminal point is at point a, it can intersect with the line A_1A_3 at point b.

Concerning the inner arc (i.e., boundary 3), according to the first distribution law, when the terminal point of $\Delta \dot{I}_n$ is at point b, I_Σ is larger than when the terminal point of $\Delta \dot{I}_n$ is at point a. Based on the second distribution law, when the terminal point of $\Delta \dot{I}_n$ is at A_1 and A_3, I_Σ is larger than when the terminal point of $\Delta \dot{I}_n$ is at point b. Therefore, if the GOS appears on the inner arc, it must be at both ends of the inner arc. As for the outer arc (i.e., boundary 4), any point on the straight line A_2A_4 is inside the fan-shaped region, making it impossible to conclude that the GOS can only appear at the two endpoints of the arc, similar to the inner arc. Hence, if the GOS is on the outer arc, it may appear anywhere on the outer arc.

B. Reduction and Discretization of NCCS

In accordance with the distribution laws of the GOS in the NCCS, the NCCS can be effectively reduced from n fan-shaped regions to n outer arcs along with 2n points, as illustrated in Fig. 8.
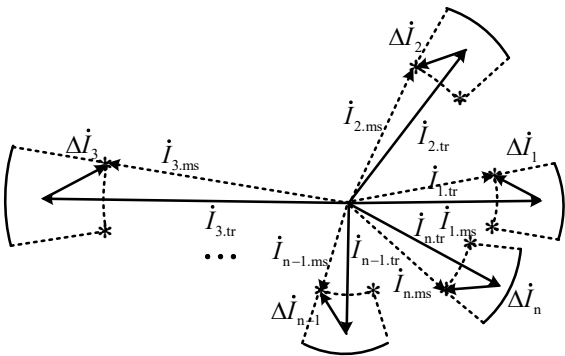

Fig. 8. The initial reduction and discretization process of the NCCS.

To further streamline and refine the outer arc from Fig. 8, we can construct the tangent of the arc via point A_2, point A_4, and the arc's apex, as depicted in Fig. 9.
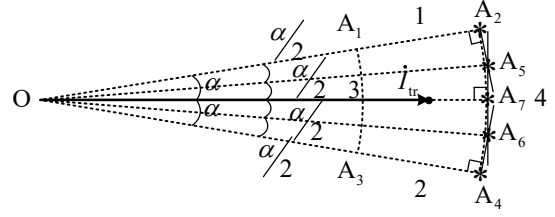

Fig. 9. Discretization process of outer arc.

It is noteworthy that the intersection of the tangent lines drawn from point A_2 and the arc's apex A_7 is denoted as A_5, while the intersection of the tangent lines from point A_4 and A_7 is labeled A_6. It is evident that both OA_5 and OA_6 serve as angular bisectors.

Given that any point on the straight lines A_2A_5, A_5A_6, and A_4A_6 exists outside the fan-shaped region, we can leverage the first and second distribution laws to reduce and discretize boundary 4 into four points: A_2, A_5, A_6 and A_4. Therefore, the NCCS can be further simplified and discretized from n outer arcs with 2n points to 6n points, as presented in Fig. 10.
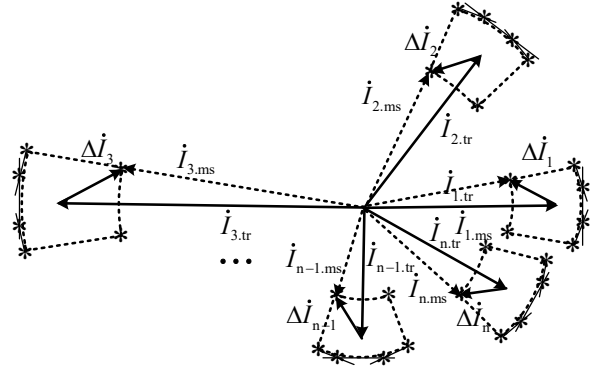

Fig. 10. The second reduction and discretization process.

However, this approach involves expanding the constraint space, resulting in only an approximation(recorded as $I_{\Sigma.max}'$) of the GOS, rather than the true GOS, with $I_{\Sigma.max}'$ having to be greater than $I_{\Sigma.max}$. The discrepancy between $I_{\Sigma.max}$ and $I_{\Sigma.max}'$ is closely tied to the distance from points on lines A_2A_5, A_5A_6, and A_4A_6 to the arc. As depicted in Fig. 9, A_5 and A_6 are the farthest points from the outer arc. With I_{tr} as a reference value, the distance per unit from A_5 and A_6 to the outer arc is determined as follows.

$$d = (1+\lambda)(\frac{1}{\cos(\alpha/2)}-1) \qquad (26)$$

It can be observed that a smaller λ and α result in a smaller d. For instance, if λ equals 5% and α equals 5°, then d equals 0.001p.u.. In this case, $I_{\Sigma.max}'$ and $I_{\Sigma.max}$ are nearly identical, and the discrepancy between them falls within an acceptable range. As λ and α increase, the discrepancy between them also grows. To address this issue, we can generate a tangent to the outer arc by intersecting OA_5 and OA_6 with the outer arc, and then discretize the outer arc more accurately, as illustrated in Fig. 11.
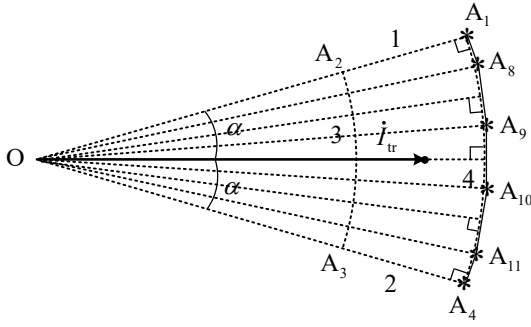
Fig. 11. High-precision discretization process of outer arc.

In Fig. 11, the intersections of the new tangents are denoted by A_8, A_9, A_{10} and A_{11}. In this scenario, A_8 to A_{11} represent the farthest points from the arc, with I_{tr} serving as the reference value and the distance per unit value being

$$d = (1+\lambda)(\frac{1}{\cos(\alpha/4)} - 1) \tag{27}$$

Compared to (26), the d decreases, and the discrepancy between $I_{\Sigma.max}'$ and $I_{\Sigma.max}$ becomes smaller. As λ and α increase, we can adopt similar methods to generate tangents continuously, determine tangent intersection points, replace arcs with multiple tangents, replace curves with straight lines, and then discretize boundary 4 into tangent intersection points via the aforementioned distribution laws. This approach allows the NCCS to be discretized into 6n, 8n, $\cdots$, (4+2m)n points ($m \geq 1$). The larger the number of points, the closer $I_{\Sigma.max}'$ is to $I_{\Sigma.max}$. However, regardless of how many points are discretized, $I_{\Sigma.max}'$ will always be slightly greater than $I_{\Sigma.max}$. Hence, even if $I_{\Sigma.max}$ cannot be obtained, $I_{\Sigma.max}'$ can still satisfy the requirements of protection setting.

C. The Solving Steps Based on Restricted Enumeration Method

Based on the aforementioned results of NCCS reduction and discretization, this paper proposes a novel restricted enumera-tion method. The specific steps are outlined as follows.

Step 1, Iuput the $I_{1.tr} \sim I_{n.tr}$ and $\beta_{1.tr} \sim \beta_{1.tr}$ values which represent the magnitude and phase of $\dot{I}_{1.tr} \sim \dot{I}_{n.tr}$ respectively. It is imperative that $\dot{I}_{1.tr} \sim \dot{I}_{n.tr}$ denotes the fault current flowing through each ISW when the most severe fault occurs outside the protected area. In accordance with (1), the ER can be deemed equivalent to a controlled voltage source, while based on (3), the IIDG can be regarded as a controlled current source. By combining the node voltage equation of the fault equivalent circuit, the short-circuit current can be calculated using an iterative method to obtain $\dot{I}_{1.tr} \sim \dot{I}_{n.tr}$. The specific calculation process is not elaborated on in this paper.

Step 2: Input $\lambda_1 \sim \lambda_n$ and $\alpha_1 \sim \alpha_n$ values. These values can be determined by employing the current transformer model and data synchronization accuracy of the data synchronization method. Then, based on $\lambda_1 \sim \lambda_n$ and $\alpha_1 \sim \alpha_n$ values, the NCCS is discretized into (4+2m)n points, generating a data matrix that will be exhaustively searched, as shown in (28).

$$\begin{bmatrix} I_{1.tr}(1-\lambda_1)\angle(\beta_{1.tr}-\alpha_1) & \cdots & I_{n.tr}(1-\lambda_n)\angle(\beta_{n.tr}-\alpha_n) \\ I_{1.tr}(1-\lambda_1)\angle(\beta_{1.tr}+\alpha_1) & \cdots & I_{n.tr}(1-\lambda_n)\angle(\beta_{n.tr}+\alpha_n) \\ I_{1.tr}(1+\lambda_1)\angle(\beta_{1.tr}-\alpha_1) & \cdots & I_{n.tr}(1+\lambda_n)\angle(\beta_{n.tr}-\alpha_n) \\ I_{1.tr}(1+\lambda_1)\angle(\beta_{1.tr}-\frac{(2k+1)\alpha_1}{2^m}) & \cdots & I_{n.tr}(1+\lambda_n)\angle(\beta_{n.tr}-\frac{(2k+1)\alpha_n}{2^m}) \\ \vdots & & \\ I_{1.tr}(1+\lambda_1)\angle(\beta_{1.tr}-\frac{\alpha_1}{2^m}) & \cdots & I_{n.tr}(1+\lambda_n)\angle(\beta_{n.tr}-\frac{\alpha_n}{2^m}) \\ I_{1.tr}(1+\lambda_1)\angle(\beta_{1.tr}+\frac{\alpha_1}{2^m}) & \cdots & I_{n.tr}(1+\lambda_n)\angle(\beta_{n.tr}+\frac{\alpha_n}{2^m}) \\ \vdots & & \\ I_{1.tr}(1+\lambda_1)\angle(\beta_{1.tr}+\frac{(2k+1)\alpha_1}{2^m}) & \cdots & I_{n.tr}(1+\lambda_n)\angle(\beta_{n.tr}+\frac{(2k+1)\alpha_n}{2^m}) \\ I_{1.tr}(1+\lambda_1)\angle(\beta_{1.tr}+\alpha_1) & \cdots & I_{n.tr}(1+\lambda_n)\angle(\beta_{n.tr}+\alpha_n) \end{bmatrix} \tag{28}$$

Where, $0 \leq k \leq 2^{m-1}-1$, $m \geq 1$.

Step 3, For the (4+2m)n rows n columns matrix in (28), various values of $x_{i1,1}$, $x_{i2,2}$, $\cdots$, $x_{in,n}$ are taken, and operations are performed $(4+2^m)^n$ times as follows.

$$I_\Sigma = \left| x_{i1,1} + x_{i2,2} + \cdots + x_{in,n} \right| \tag{29}$$

Where, $1 \leq i1$, $i2$, $\cdots$, $i_n \leq 4+2^m$.

Step 4: The maximum value is found among the $(4+2^m)^n$ results obtained in Step 3, which represents the approximate solution(i.e, $I_{\Sigma.max}'$) of the GOS. $I_{\Sigma.max}'$ is then substituted for $I_{\Sigma.max}$ to be set as the protection setting value in (10).

V. CASE STUDY

Based on the FWIDNs system topology depicted in Fig. 14, a simulation model has been developed in PSCAD/EMTDC.
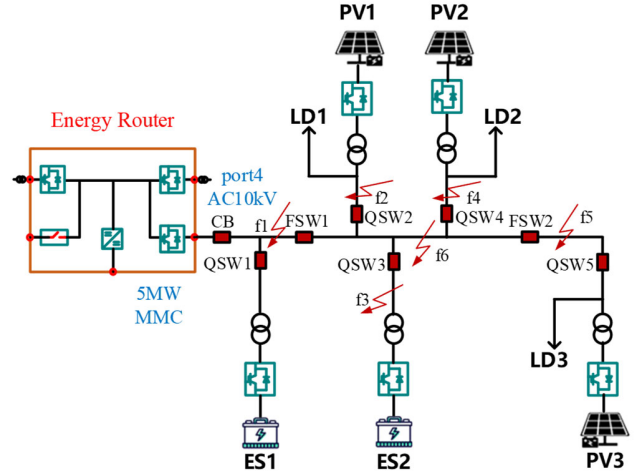

Fig. 12. The system topology of FWIDNs.

The system operates under the neutral point ungrounded mode with ER 10kV interface capacity of 5MW and a rated frequency of 50Hz. The ER adopts the V/f control strategy during normal operation and switches to the current dependent voltage order limiter in the event of a fault. The current limiting control parameters, I_{cdvol}^{ref} and k, are set to 1.05p.u. and 1, respectively. The maximum fault current magnitude, can be calculated using (2) to be 2.05p.u. The rated capacity of

PV1~PV3 and ES1~ES2 is 1MW. Prior to a fault, the IIDGs employ the PQ control strategy to output 1p.u. power at the unit power factor, while after a fault, they switch to negative sequence current suppression and LVRT control strategies, taking into consideration fault current limiting. The line impedance is set to $Z_1 = 0.1 + j0.3\,\Omega/\text{km}$ and $Z_0 = 0.3 + j0.9\,\Omega/\text{km}$, with a T-connected line length of 1km and the length of the line between adjacent T-connected lines at 2km. LD1~LD3 are rated at 2MW. As an example, a set of MTCDP composed of FSW1, FSW2, and QSW2~QSW4 is utilized. Faults outside the protected area, f1~f5, are distinguished from faults inside the protected area, f6.

A. The Weak-Infeed Properties of ER and IIDGs

In this paper, we focus on analyzing the output fault current waveforms of the ER and PV1 under a three-phase short circuit at point f6, as shown in Fig.13. It is worth noting that the output fault current waveforms of PV2, PV3, ES1 and ES2 exhibit a similar pattern to that of PV1, and are not discussed in detail here.
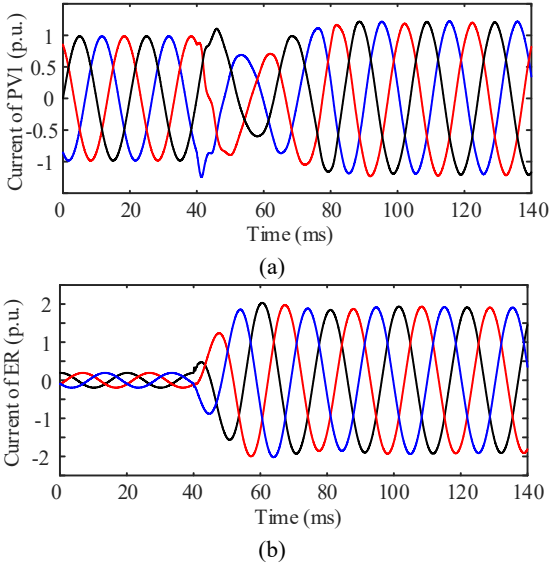

Fig. 13. Fault current waveforms. (a) PV1, (b) ER.

As depicted in Fig. 13, the ER's fault current undergoes a short transient stage lasting 2~3 cycles, before entering a steady-state fault stage where it does not exceed 2 times the rated current. This result is in stark contrast to the fault current of the main power supply of traditional DNs, as the ER exhibits a weak-infeed characteristic. Additionally, under the LVRT control strategy, the fault output current of IIDG does not exceed 1.2 times the rated value, and all power supplies in the DNs demonstrate weak-infeed characteristics.

To further understand the characteristics of the FWIDNs, we calculate the steady-state fault current when the fault occurs at f1~f5 and the fault current at each ISW, as illustrated in Table I. Here only shows the results of A-phase, with the A-phase current of FSW1 serving as the reference.

From Table I, it is evident that regardless of the fault location, the current with the highest magnitude flowing through each ISW does not exceed four times the sum of the

three-terminal current with the lowest magnitude. This observation indicates that the differential current in the FWIDNs is linked to the multi-terminal current errors.

TABLE I
CALCULATED STEADY-STATE FAULT CURRENT VALUES FOR EACH ISW DURING THREE-PHASE SHORT-CIRCUIT FAULTS AT VARIOUS LOCATIONS

		FSW1	QSW2	QSW3	QSW4	FSW2
f1	mag(kA)	0.2761	0.0694	0.0693	0.0698	0.0699
	phase(°)	0.0	198.6	184.9	170.2	166.7
f2	mag(kA)	0.6116	0.4092	0.0693	0.0694	0.0695
	phase(°)	0.0	183.1	189.4	168.8	163.3
f3	mag(kA)	0.5957	0.0699	0.5155	0.0693	0.0694
	phase(°)	0.0	-36.2	176.9	179.8	169.1
f4	mag(kA)	0.5754	0.0716	0.0693	0.6268	0.0693
	phase(°)	0.0	-39.8	-27.6	173.6	173.3
f5	mag(kA)	0.5537	0.0743	0.0693	0.0700	0.7320
	phase(°)	0.0	-47.6	-27.4	-38.2	169.8

B. The Validity Verification of The Proposed Restrictive Enumeration Method

Generally, for 10kV distribution network protection, it is recommended to use Class P current transformers(CT). The accuracy class 10P protection CT has a magnitude error of 3% at the rated primary current and an error of 10% at the rated accuracy limit primary current (which can be 20 times the rated current). Considering 10% error is high due to the limited magnitude of the fault current in the analyzed FWIDNs. Thus, we made a compromise between 10% and 3% and decided to set the magnitude error to 5%.

When using fiber optic communication, with data transmission speed of 2×10^5 km/s in the fiber, the data transmission delay for every 10 km length of fiber is about 50μs, corresponding to a sampling angular error of 0.9°. For the accuracy class 10P protection CT, when the magnitude error is 10%, the phase error is generally considered to be 7°. However, considering the limited magnitude of the fault current in the analyzed FWIDNs, setting the phase error to 7° is high. Thus, we made a compromise and set the current transformer phase error to 4°, and considered an additional 1° error for fiber optic communication synchronization, resulting in a total phase error of 5°.

It's important to note that the proposed method is not limited to specific magnitude and phase errors. This method is applicable regardless of the values of magnitude and phase errors.

This study assumes a maximum magnitude error of 5% and a maximum phase error of 5° for measured terminal currents. To calculate the maximum differential current superimposed on multi-terminal current phasor errors, exhaustive search methods are performed on the entire fan-shaped shadow

region and on its boundary, recorded as exhaustive search method 1 and exhaustive search method 2, respectively. Where, the exhaustive search method 1 means that in the entire fan-shaped shadow region, 121 feasible solutions are taken at an interval of 0.01 p.u. per magnitude and 1° per phase. And exhaustive search method 2 means that on the boundary of the fan-shaped shadow region, the straight line boundary takes 20 feasible solutions at an interval of 0.01 p.u. per magnitude, and the arc boundary takes 20 feasible solutions at an interval of 1° per phase. The results and time consumption of these methods are compared with the proposed restricted enumeration method, as shown in Table II. The proposed restricted enumeration method discretizes the NCCS into 6n, 8n, and 12n points, respectively.

The algorithm program is written in Matlab 2020b for calculation, and the computations are performed on a computer equipped with an Intel (R) Core (TM) i7-6700HQ CPU @ 2.60GHz 2.59GHz processor.

Considering the limited measurement accuracy of the CT, we can only be precise up to 0.0001kA. From the results, exhaustive search method 1 and method 2 yield the same results, successfully verifying the correctness of distribution law 1. Furthermore, the results of exhaustive search method 1 and the 6n, 8n, and 12n points restricted enumeration method are identical, successfully verifying the effectiveness of the proposed restricted enumeration method and the three distribution laws of the optimal solution in the NCCS. The calculation time in Table II shows that the proposed restricted enumeration method is much faster than the direct exhaustive search, with a time consumption that is 4~5 orders of magnitude lower, indicating that the proposed method is capable of meeting the protection setting needs.

TABLE II
MAXIMUM DIFFERENTIAL CURRENT CALCULATION RESULTS AND COMPUTATION TIMES FOR THREE-PHASE SHORT-CIRCUIT FAULTS AT DIFFERENT LOCATIONS USING VARIOUS CALCULATION METHODS.

	Exhaustive Search Method 1		Exhaustive Search Method 2		12n Points Restricted Enumeration		8n Points Restricted Enumeration		6n Points Restricted Enumeration	
	results(kA)	time(s)	results(kA)	time(s)	results(kA)	time(s)	results(kA)	time(s)	results(kA)	time(s)
f1	0.0546	3856.143	0.0546	27.845	0.0546	0.153	0.0546	0.061	0.0546	0.048
f2	0.1228	3890.706	0.1228	28.123	0.1228	0.148	0.1228	0.068	0.1228	0.059
f3	0.1324	3921.284	0.1324	26.795	0.1324	0.151	0.1324	0.071	0.1324	0.061
f4	0.1410	4013.446	0.1410	27.261	0.1410	0.146	0.1410	0.062	0.1410	0.058
f5	0.1501	3920.861	0.1501	27.339	0.1501	0.139	0.1501	0.066	0.1501	0.053

C. The Reliability and Sensitivity Analysis of The Proposed MTCDP Setting Method for FWIDNs

In order to ensure that the protection does not maloperation when a fault occurs outside the protection area, the maximum value of the maximum differential current should be selected when a three-phase short-circuit fault occurs at different locations. This value should then be multiplied by the reliability coefficient $k_{rel} = 1.1$ to determine the I_{set}.

$$I_{set} = k_{rel} I_{\Sigma.max} = 1.1 \times 0.1501 = 0.1651 \text{ kA} \quad (30)$$

To analyze the reliability of the proposed protection setting method, we conduct three-phase short-circuit fault simulations at locations f1 to f5 in the simulation model of FWIDNs. Based on the simulated fault currents at each ISW, we add magnitude errors of ±5% and phase errors of ±5°, creating 4 different measurement values for each of the 5 terminal currents. This resulted in a total of 1024 possible I_{diff}. The results of comparing the I_{diff} with I_{set} during three-phase short-circuit faults occurring at different locations under the proposed method are presented in Fig. 14.

The vertical axis represents the magnitude of I_{diff} and I_{set}, while the horizontal axis represents the identification numbers for the 1024 cases.
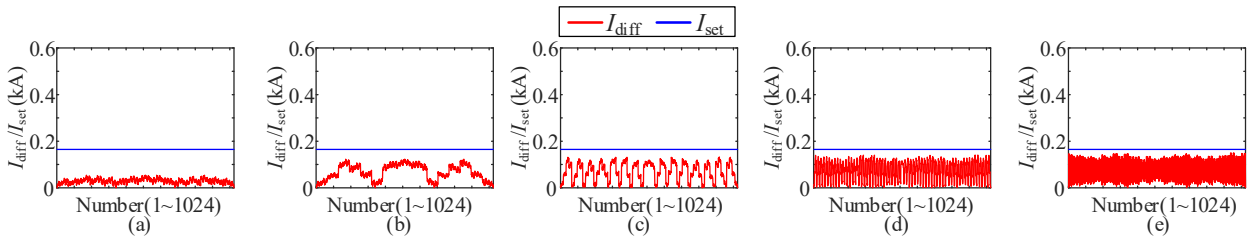

Fig. 14. The simulation results of the proposed method for I_{diff} and I_{set}. (a) Fault at f1, (b) Fault at f2, (c) Fault at f3, (d) Fault at f4, (e) Fault at f5.

As shown in Fig. 14, the I_{diff} are all less than the I_{set} when a three-phase short-circuit fault occurs at different locations outside the protection area. The protection does not maloperation. The proposed method has good reliability.

To evaluate the sensitivity of the proposed protection setting method, AB phase-to-phase faults were set at f6 in the protection zone of the simulation model, with transition resistance of 40Ω.

Regarding asymmetric faults, IIDGs typically suppress negative sequence currents to zero. In order to reduce the operational challenges of LVRT for IIDGs and mitigate the adverse effects of asymmetric faults on the DNs, the control objective of ER should be to maximize the positive sequence voltage and minimize the negative sequence voltage. During asymmetric faults with high transition impedance, the negative sequence control objective of ER can be to suppress the negative sequence voltage at the 10kV interface to 0, while the reference value for positive sequence voltage is determined by the current dependent voltage order limiter in equation (1). Under such control strategy, the simulated waveforms of ER's fault electrical quantities are shown in Fig. 15.

(a)

(b)
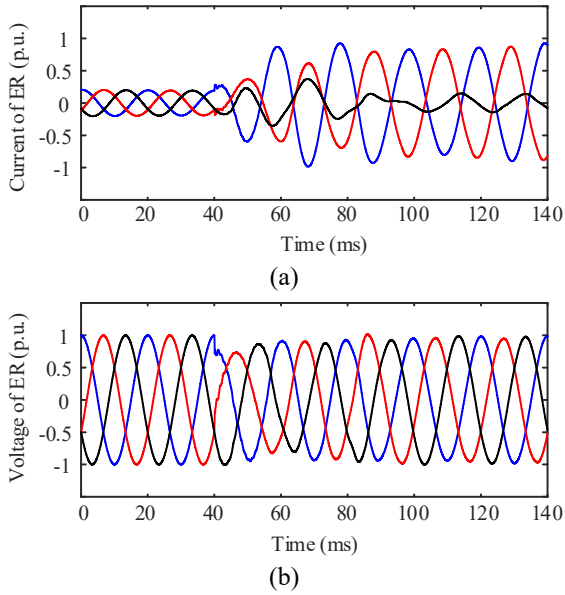
Fig. 15. The simulated waveforms of ER's fault electrical quantities. (a) Output current, (b) Interface voltage.

From Fig. 15, it can be observed that when the transition resistance is 40Ω and using the control strategy of suppressing negative sequence voltage to 0, the ER interface voltage remains three-phase symmetrical. Moreover, the $I_{ER.abc}^{max}$ is 0.9 p.u., which does not exceed the I_{cdvol}^{ref}. The positive sequence voltage is still maintained at the rated level.

The simulated waveforms of PV1's fault electrical quantities are shown in Fig. 16.

The fault electrical quantity waveforms of other IIDGs are similar to PV1, and they are not shown here. From Fig. 16, it can be observed that the grid-connected voltage of PV1 is essentially the same as the ER interface voltage. When the transition resistance is 40Ω, the grid-connected voltage of PV1 quickly recovers to the rated level after a transient period of a few cycles, and the three-phase output current of PV1 also temporarily increases and then returns to the pre-fault level. PV1 seems to be oblivious to the presence of the fault, indicating that the ER's negative sequence voltage suppression control strategy has achieved the goal of reducing the operational challenges of IIDG during LVRT and weakening the adverse effects of unsymmetrical faults on the DNs.
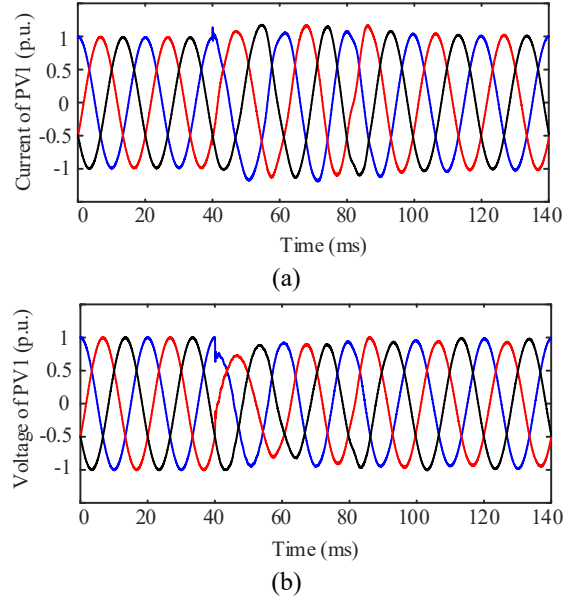

(a)

(b)

Fig. 16. The simulated waveforms of PV1's fault electrical quantities. (a) Output current, (b) Grid-connected voltage.

The three-phase currents at each ISW during the AB phase-to-phase short-circuit fault with a transition resistance of 40Ω in the protection zone are shown in Table III.

TABLE III
THE THREE-PHASE CURRENTS AT EACH ISW DURING THE AB PHASE-TO-PHASE SHORT-CIRCUIT FAULT WITH A TRANSITION RESISTANCE OF 40Ω IN THE PROTECTION ZONE

		FSW1	QSW2	QSW3	QSW4	FSW2
mag(kA)	A	0.3332	0.0563	0.0586	0.0554	0.0551
	B	0.3149	0.0510	0.0584	0.0474	0.0471
	C	0.1076	0.0561	0.0585	0.0550	0.0547
phase(°)	A	13.6	174.8	-3.6	171.4	171.1
	B	-147.6	57.6	-123.6	55.5	55.2
	C	122.7	-59.2	116.5	-59.4	-59.8

Based on the simulated fault current values at each ISW in Table III, we added magnitude errors of ±5% and phase errors of ±5°. This was done to simulate the fault current measurement values at each ISW. For each of the 5 terminal currents, 4 different measurement values can be simulated, resulting in a total of 1024 possible I_{diff}. The simulation results are shown in Fig. 17.
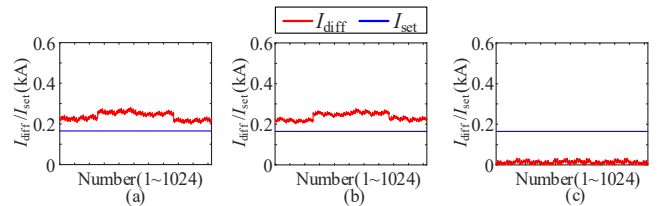

Fig. 17. The results of comparing the I_{diff} with I_{set} under the proposed method. (a) A phase, (b) B phase, (c) C phase.

The simulation results indicate that when the transition resistance is 40Ω, the differential currents of the faulted phases are all greater than the protection set value of 0.1651kA. Thus, the differential protection reliably operates. In other words, the differential protection does not fail when the transition resistance is 40Ω.

Moreover, a large number of examples were analyzed by randomly adding magnitude errors within ±0.05p.u. and phase errors within ±5° to simulation values to simulate measured values the in the simulation of different fault locations and types. The results demonstrate that the MTCDP setting method proposed in this paper has sufficient sensitivity and reliability in FWIDNs.

D. The Reliability and Sensitivity Analysis of The Existing MTCDP Setting Methods for FWIDNs

The existing MTCDP schemes follow the approach of first transforming the multi-terminal currents into equivalent double-terminal currents using certain methods, then applying double-terminal CDP settings, mostly incorporating protective criteria with restraining quantities. As a comparison to the method proposed in this paper, we conducted performance tests on the MTCDP criteria and setting methods from references [17-20] in FWIDNs.

The fault current simulation values and measurement values at each ISW were consistent with the data used earlier for the reliability and sensitivity analysis of the proposed MTCDP setting method for FWIDNs.

The simulation results of the reference [17-20] methods for differential current I_{diff} and restraining current I_{res} during three-phase short-circuit faults occurring at different locations outside the protection zone are shown in Fig. 18 to Fig. 21.
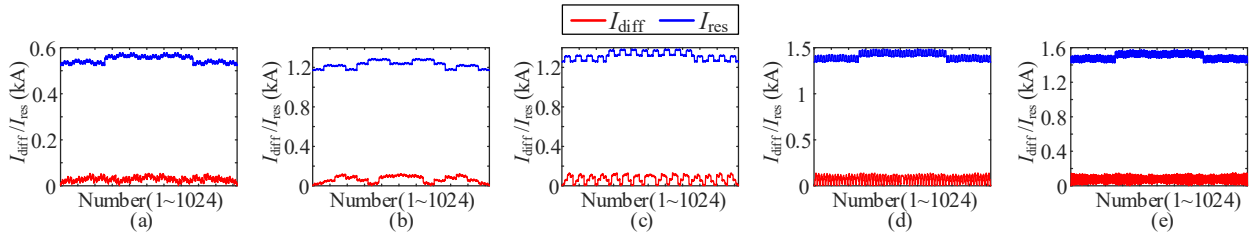

Fig. 18. The simulation results of the reference [17] method for I_{diff} and I_{res}. (a) Fault at f1, (b) Fault at f2, (c) Fault at f3, (d) Fault at f4, (e) Fault at f5.
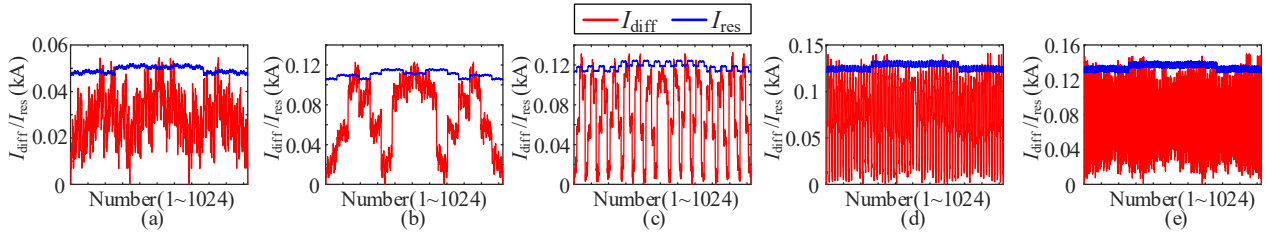

Fig. 19. The simulation results of the reference [18] method for I_{diff} and I_{res}. (a) Fault at f1, (b) Fault at f2, (c) Fault at f3, (d) Fault at f4, (e) Fault at f5.
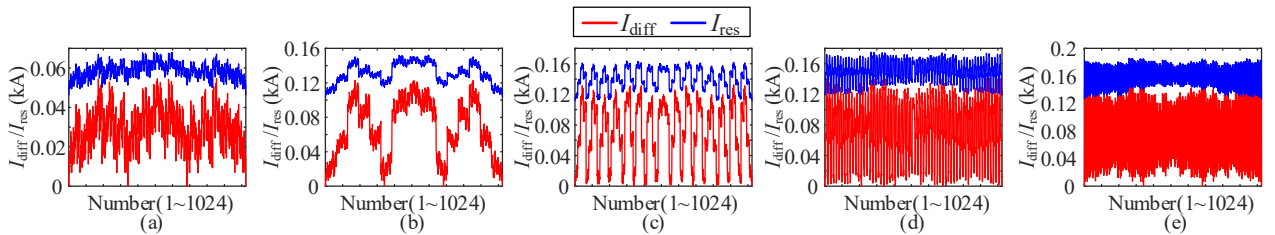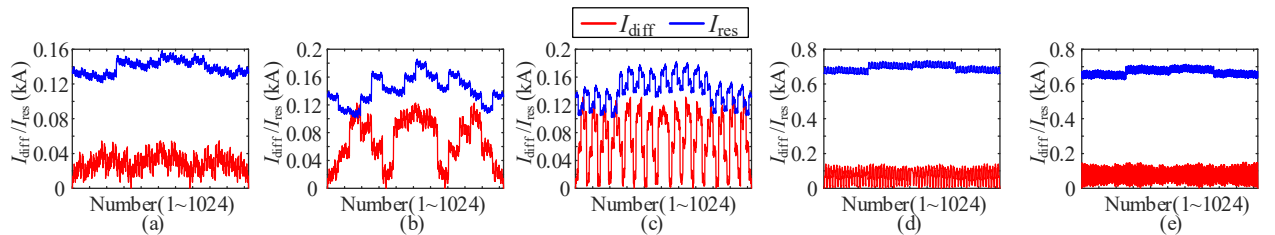

Fig. 20. The simulation results of the reference [19] method for I_{diff} and I_{res}. (a) Fault at f1, (b) Fault at f2, (c) Fault at f3, (d) Fault at f4, (e) Fault at f5.

Fig. 21. The simulation results of the reference [20] method for I_{diff} and I_{res}. (a) Fault at f1, (b) Fault at f2, (c) Fault at f3, (d) Fault at f4, (e) Fault at f5.

From Fig. 18, it is evident that the method proposed in [17] consistently ensures I_{diff} remains below I_{res}, thereby indicating that the protection will not maloperate. From Fig. 19, it can be observed that under the method proposed in [18], there are instances where I_{diff} exceeds I_{res}, indicating a potential risk of maloperation for the protection. From Fig. 20 (d) and (e), it is apparent that under the method proposed in [19], there are scenarios where I_{diff} surpasses I_{res}, signaling a potential risk of maloperation for the protection. From Fig. 21 (b) and (c), it can be observed that under the method proposed in [20], there are situations where I_{diff} exceeds I_{res}, suggesting a potential risk of maloperation for the protection.

The simulation results of the reference [17-20] methods for I_{diff} and I_{res} during AB phase-to-phase short-circuit fault with a transition resistance of 40Ω occurring inside the protection zone are shown in Fig. 22 to Fig. 25.
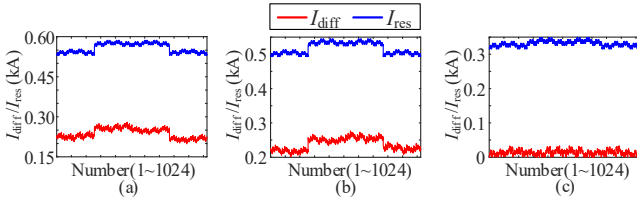

Fig. 22. The simulation results of the reference [17] method for I_{diff} and I_{res}. (a) A phase, (b) B phase, (c) C phase.
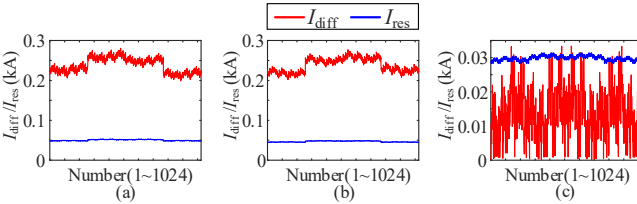

Fig. 23. The simulation results of the reference [18] method for I_{diff} and I_{res}. (a) A phase, (b) B phase, (c) C phase.
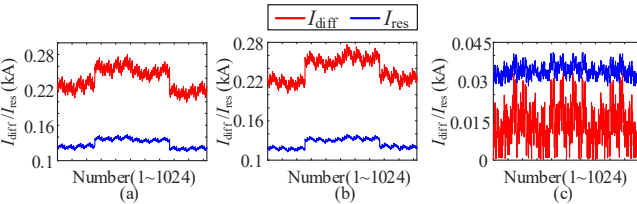

Fig. 24. The simulation results of the reference [19] method for I_{diff} and I_{res}. (a) A phase, (b) B phase, (c) C phase.
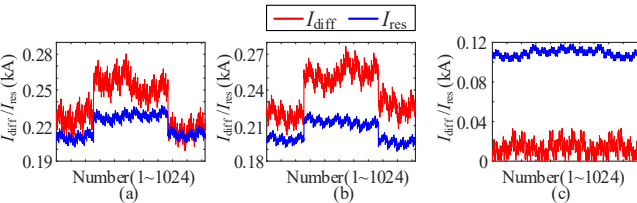

Fig. 25. The simulation results of the reference [20] method for I_{diff} and I_{res}. (a) A phase, (b) B phase, (c) C phase.

In Fig. 22, it is evident that the method proposed in [17] causes the I_{diff} of the faulted phase to always be less than I_{res}, resulting in protection refusing to operate. From Fig. 23, it can be observed that the method proposed in [18] leads to the I_{diff}

of the faulted phase being greater than I_{res}, allowing the protection to operate correctly. In Fig. 24, it is apparent that the method proposed in [19] results in the I_{diff} of the faulted phase being greater than I_{res}, enabling the protection to operate correctly. From Fig. 25 (a) and (b), it can be observed that the method proposed in [20] may lead to cases where the I_{diff} of the faulted phase is less than I_{res}, indicating a risk of protection refusing to operate.

In summary, the methods proposed in references [17-20] generally perform correctly in a majority of cases. However, there are certain scenarios where they may either refuse to operate or misoperate, thus failing to meet the requirements of MTCDP in FWIDNs. Consequently, we can deduce that, when compared to the methods presented in references [17-20], the method proposed in this paper demonstrates superior reliability and sensitivity in FWIDNs.

E. The Evaluation of The Impact of Transient Events on The Proposed Protection Scheme

We conducted an evaluation of the impact of transient events, such as transformer energization, heavy load switching, and induction motor starting, on the proposed protection scheme. These transient events all occur outside the protection zone. Thus, the evaluation objective is to determine whether these transient events could cause protection maloperation.

During transformer energization, a significant excitation inrush current (EIC) with a large magnitude occurs due to severe core saturation. The peak magnitude of this EIC can reach 6 to 8 times the rated current of the transformer. We performed simulation analysis using a 2000kVA 10kV/0.4kV transformer as an example, which is considered relatively large in a 10kV DNs.

Under an ideal 10kV AC voltage source, the transformer is energized at the moment when one phase of the voltage is passing through zero. The voltage and EIC waveforms are shown in Fig. 26.
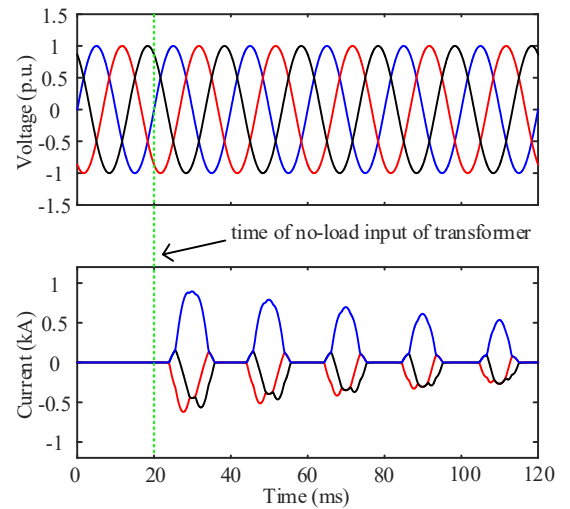

Fig. 26. The voltage and excitation inrush current waveforms of a transformer during energization under an ideal 10kV AC voltage source.

From Fig. 26, it can be observed that the maximum peak magnitude of the EIC reaches around 0.9kA, nearly 8 times the rated current of the transformer.

However, in FWIDNs, the ER and IIDGs serve as power-electronic-based weak sources, which differ significantly from the ideal source. In Fig. 12, we replaced a 2MW load with a 2000kVA 10kV/0.4kV transformer at location LD1. We conducted simulation analysis of the EIC during transformer energization in FWIDNs. The transformer is energized at the moment when one phase of the voltage is passing through zero. The voltage and EIC waveforms are shown in Fig. 27.
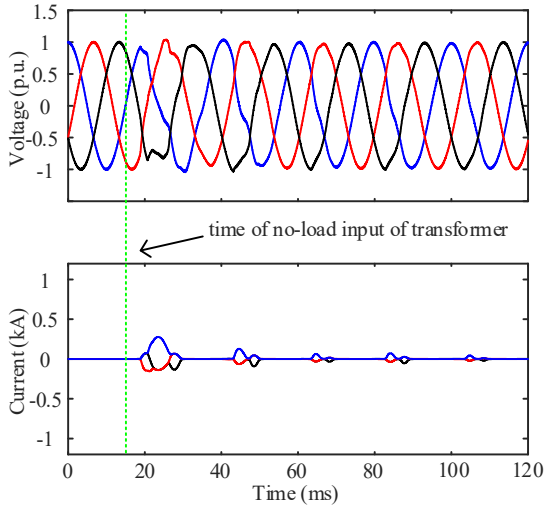

Fig. 27. The voltage and excitation inrush current waveforms of a transformer during energization in FWIDNs.

It can be observed that, the EIC during transformer energization shows significant differences between an ideal voltage source and FWIDNs, despite the identical excitation characteristics and parameter settings for the transformer. Under the ideal voltage source, the EIC exhibits a large peak magnitude. However, in FWIDNs, during transformer energization, the voltage at the transformer connection point experiences transient fluctuations of around 2 cycles, which play a role in suppressing the EIC. As a result, the EIC during transformer energization in FWIDNs is only about 0.28kA.

Based on the fault current simulation values at each ISW for the first few cycles after transformer energization, we simulated the fault current measurement values and differential currents the same approach as described earlier. The simulation results of the I_{diff} are presented in Fig. 28.
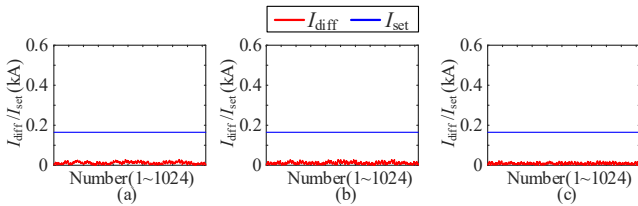

Fig. 28. The results of comparing the I_{diff} with I_{set} during transformer energization. (a) A phase, (b) B phase, (c) C phase.

As can be seen from the Fig. 28, during transformer energization, I_{diff} is always smaller than I_{set}, indicating that the protection will not maloperate.

Induction motors are known for the significant consumption of reactive power, and their individual capacities in DNs are typically not very large. For instance, motors used in machines and water pumps range from several kW to several MW. When employing direct starting, the induction motor experiences its maximum starting current, which is generally 4 to 7 times the rated current of the motor. To minimize the impact of starting currents on the power grid, direct starting is commonly used for smaller capacity motors with lighter loads. However, large capacity motors with heavy loads often adopt wound rotor induction motors, where additional rotor resistance can be introduced to reduce the starting current and increase the starting torque..

To analyze the impact of induction motor starting on protection, we focused on large capacity induction motors. Specifically, we considered a wound rotor induction motor with a rated capacity of 2MVA and operating at its rated load. In the simulation, we replaced the 2MW load at location LD1 in Fig. 12 with the 2MVA wound rotor induction motor. The parameters of the induction motor, such as the stator and rotor resistances, stator and rotor leakage reactances, excitation reactance, and additional rotor resistance at 10kV side, were set at 0.043 p.u., 0.04 p.u., 0.06 p.u., 0.06 p.u., 4 p.u., and 0.2 p.u., respectively. The voltage and starting current at the motor terminal during its starting process are shown in Fig. 29.
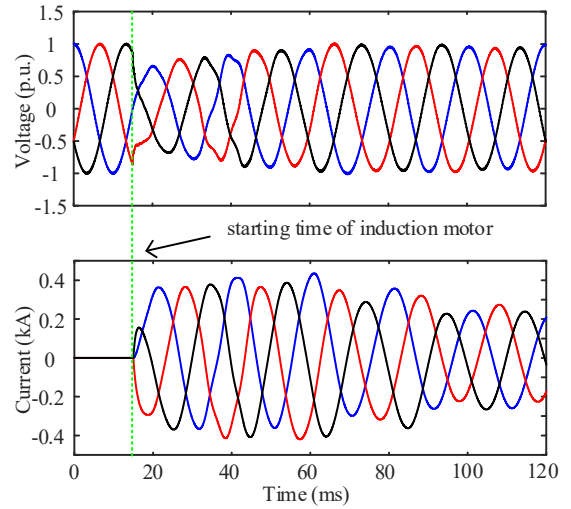

Fig. 29. The voltage and starting current waveforms of the induction motor during its starting process.

From Fig. 29, it can be observed that in FWIDNs, during the starting process of a large-capacity induction motor with heavy load, there is a certain degree of temporary voltage dip, and the starting current reaches around 0.43kA, approximately 2.6 times the rated current of the induction motor.

Based on the fault current simulation values at each ISW after the induction motor starts, we simulated the fault current measurement values and I_{diff} using the same approach as

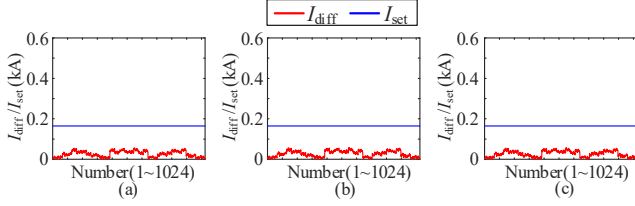described earlier. The simulation results of the I_{diff} are shown in Fig. 30.

Fig. 30. The results of comparing the I_{diff} with I_{set} during the induction motor starting. (a) A phase, (b) B phase, (c) C phase.

From Fig. 30, it can be observed that during the starting process of the induction motor, I_{diff} is always less than I_{set}, indicating that the protection will not maloperate.

The electrical quantity simulation waveforms for the heavy load input and output scenario are shown in Fig. 31, using the 2MW load at location LD1 in Fig. 12 as an example.
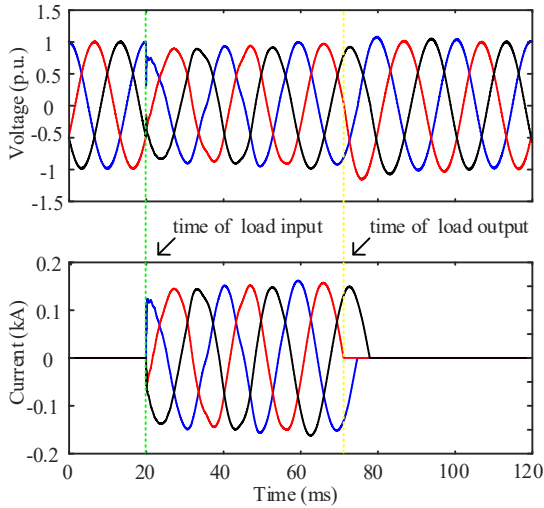

Fig. 31. The voltage and current waveforms during heavy load input and output scenario.

Fig. 31 shows that heavy load input and output result in temporary voltage drops and rises at the load connection point, along with corresponding changes in current. However, our protection tripping criteria do not consider voltage quantity, so the voltage fluctuations do not cause any false tripping of the protection. The load current reaches around 0.16kA.

Based on the fault current simulation values at each ISW after heavy load input, we simulated the fault current measurement values and I_{diff} using the same method as before. The simulation results of the I_{diff} are shown in Fig. 32.
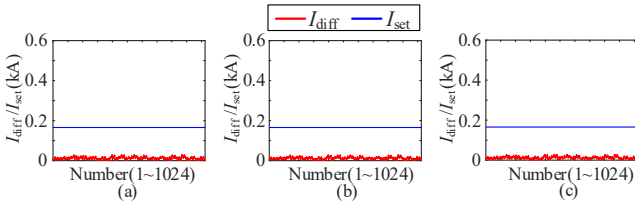

Fig. 32. The results of comparing the I_{diff} with I_{set} during the heavy load input. (a) Phase A, (b) Phase B, (c) Phase C.

From Fig. 32, it can be observed that during the heavy load input, I_{diff} is always smaller than I_{set}, indicating that the protection will not maloperate.

In conclusion, in FWIDNs, the proposed protection scheme demonstrates excellent reliability during transient events such as transformer energization, heavy load input and output, and induction motor starting, as it does not cause any false tripping.

VI. CONCLUSION

This paper introduces a novel MTCDP setting method for FWIDNs based on a restricted enumeration approach. The main contributions and innovations of this paper are highlighted as follows.

(1) The weak-infeed characteristics of ER and IIDG in FWIDNs have been thoroughly examined. To mitigate the impact of multi-terminal current measurement errors and data synchronization errors on differential current, the problem of determining the maximum differential current superimposed with multi-terminal current phasor errors has been transformed into a high-dimensional non-convex optimization problem.

(2) By conducting an in-depth analysis of the distribution law of GOS in a NCCS, a restricted enumeration method has been proposed to efficiently determine the approximate GOS that satisfies the protection setting requirements. This method effectively resolves the issue of determining the MTCDP setting value in FWIDNs.

(3) The proposed protection setting method has been subject to reliability verification and sensitivity verification under fault conditions both inside and outside the protected area. The results demonstrate that the proposed method operates reliably without malfunctions when faults occur outside the protected area, and exhibits robust resistance to transition resistance when faults occur inside the protected area. When transient events such as transformer energization and induction motor starting occur outside the protection zones, the protection can reliably avoid false tripping. By comparing the simulation results of the proposed method with existing methods, the superior performance of the proposed method in FWIDNs is verified.

The MTCDP setting method proposed in this paper is applicable to the FWIDNs discussed herein and offers significant reference value for other forms of fully power-electronized power systems. It is worth noting that, when establishing a mathematical model to solve for the maximum differential current problem, only the impact of measurement errors and data synchronization errors on differential current has been considered. In future research, it is recommended to comprehensively analyze other influencing factors for a more comprehensive understanding.

REFERENCES

[1] Z. Zhang, C. Kang. "Challenges and Prospects for Constructing the New-type Power System Towards a Carbon Neutrality Future," Proc. CSEE, vol. 42, no. 8, pp. 2806-2818, Apr. 2022.

[2] T. Adefarati and R. C. Bansal, "Integration of renewable distributed generators into the distribution system: A review," IET Renew. Power Gener., vol. 10, no. 7, pp. 873–884, Aug. 2016.

[3] Q. Wang, N. Zhou and L. Ye, "Fault Analysis for Distribution Network With Current-Controlled Three-Phase Inverter-Interfaced Distributed Generators," in IEEE Transactions on Power Delivery, vol. 30, no. 3, pp. 1532-1542, June 2015.

[4] X. Kong, Z. Zhang, X. Yin, et al., "Study on fault current characteristics and fault analysis method of power grid with inverter interfaced distributed generation", Proc. CSEE, vol. 33, no. 34, pp. 65-74, Dec. 2013.

[5] T. Bi, B. Yang, K. Jia, et al., "Review on Renewable Energy Source Fault Characteristics Analysis," in CSEE Journal of Power and Energy Systems, vol. 8, no. 4, pp. 963-972, July 2022.

[6] B. Liu et al., "An AC–DC Hybrid Multi-Port Energy Router With Coordinated Control and Energy Management Strategies," in IEEE Access, vol. 7, pp. 109069-109082, 2019, doi: 10.1109/ACCESS.2019. 2933469.

[7] J. Miao, N. Zhang, C. Kang, J. Wang, Y. Wang and Q. Xia, "Steady-State Power Flow Model of Energy Router Embedded AC Network and Its Application in Optimizing Power System Operation," in IEEE Transactions on Smart Grid, vol. 9, no. 5, pp. 4828-4837, Sept. 2018, doi: 10.1109/TSG.2017.2672821.

[8] L. Huang, C. Zong, X. Yang, W. Chen, Y. Zhu and K. Bi, "Power Flow Calculation of Distribution Network With Multiple Energy Routers," in IEEE Access, vol. 9, pp. 23489-23497, 2021, doi: 10.1109/ ACCESS. 2020.3046671.

[9] Yang J , Mao S , Li X , et al. Influence Mechanism and Suppression Control of the MMC on Short-Circuit Current under AC Faults[J]. IEEE Access, 2020, PP(99):1-1.

[10] C. J. Mozina, "Impact of smart grids and green power generation on distribution systems, " IEEE Trans. Ind. Appl., vol. 49, no. 3, pp. 1079–1090, May/Jun. 2013.

[11] K. I. Jennett, C. D. Booth, F. Coffele, and A. J. Roscoe, "Investigation of the sympathetic tripping problem in power systems with large penetrations of distributed generation, "IET Gener. Transm. Distrib., vol. 9, no. 4, pp. 379–385, Mar. 2015.

[12] H. Gao, J. Li and B. Xu, "Principle and Implementation of Current Differential Protection in Distribution Network With High Penetration of DGs," in IEEE Transactions on Power Delivery, vol. 32, no. 1, pp. 565-574, Feb. 2017.

[13] X. Liu, Y. Li, "Effect of IIDG Connected to Grid as a Teed Line on Longitudinal Differential Protection and Maximum Penetration Capacity, " Power System Technology, vol.40, no. 5, pp. 1595-1600, May 2016.

[14] X. Liu, Y. Li, et al.," An Improved Scheme of Longitudinal Differential Protection for Teed Lines With Inverter-Based Distributed Generations, " Power System Technology, vol.40, no. 4, pp. 1257-1254, Apr. 2016.

[15] B. Han, H. Li, G. Wang, D. Zeng and Y. Liang, "A Virtual Multi-Terminal Current Differential Protection Scheme for Distribution Network With Inverter-Interfaced Distributed Generators," in IEEE Transactions on Smart Grid, vol. 9, no. 5, pp. 5418-5431, Sept. 2018.

[16] Q. Wang, Z. Bo, Y. Zhao, L. Wang, S. Ding and F. Wei, "Influence on the performance of multi-terminal differential protection caused by communication time desynchronizing," 2015 5th International Conference on Electric Utility Deregulation and Restructuring and Power Technologies (DRPT), 2015, pp. 943-946, doi: 10.1109/DRPT.2015. 7432364.

[17] H. Miller, J. Burger, N. Fischer and B. Kasztenny, "Modern line current differential protection solutions", Proc. 63rd Annu. Conf. Protective Relay Engineers, pp. 1-25, Mar. 2010.

[18] K. M. Silva and R. G. Bainy, "Generalized alpha plane for numerical differential protection applications", IEEE Trans. Power Del., vol. 31, no. 6, pp. 2565-2566, Dec 2016.

[19] R. G. Bainy and K. M. Silva, "Enhanced Generalized Alpha Plane for Numerical Differential Protection Applications," in IEEE Transactions on Power Delivery, vol. 36, no. 2, pp. 587-597, April 2021, doi: 10.1109/ TPWRD.2020.2985019.

[20] H. Pu, T. Wu, G. Yao, et al., "Practical Scheme of Line Differential Protection for Active Distribution Network Based on 5G Communication, " Automation of Electric Power Systems, vol. 46, no. 23, pp. 117-124, Dec. 2022.

[21] N. Jin, Z, Yu, X. Lin, et al., " Study of Multi-terminal Wide-area Current Differential Protection Criterion With High Sensitivity and Ability of Tolerating Additional Phase-shift Error," Proc. CSEE, vol. 38, no. 21, pp. 6314-6323, Nov. 2018.

[22] N. Jin, X. Lin, et al., "Research on Multiterminal Current Differential Protection Criterion With High Sensitivity and Synchronization Error Tolerance Capability," in IEEE Transactions on Power Delivery, vol. 33, no. 6, pp. 3085-3094, Dec. 2018.

[23] L. Zhen, K. Jia, T, Bi, et al., " AC-side fault analysis of a VSC-HVDC transmission system connected to offshore wind farms and the impact on protection," Power System Protection and Control, vol. 49, no. 20, pp. 20-32, Oct., 2021.